# Chromosome model reveals dynamic redistribution of DNA damage into nuclear sub-domains

Sylvain V. Costes[1], Artem Ponomarev[2,3], James L. Chen[1], Francis A. Cucinotta[2], Mary Helen Barcellos-Hoff[1]

1. Life Sciences Division, Lawrence Berkeley National Laboratory, Berkeley, CA 94720

2. NASA JSC, 2101 NASA Parkway, build. 37, mail code SK, Houston, TX 77058

3. USRA, 3600 Bay Area Blvd., Houston, TX 77058

**Corresponding Author: Sylvain Costes**

**Pages: 20**

**Word Count: 6503**

**Figures: 9**

**Key Words:** multi-scale modeling, phosphorylation foci, chromatin, double-strand breaks

**Abbreviations:**

RIF: Radiation-induced foci

DSB: Double strand break

IR: Ionizing radiation

Post-IR: Following exposure to ionizing radiation

ATM: Ataxia telangectasia mutated

ATMp: ATM phosphorylated at serine 1981

γ-H2AX: histone H2AX phosphorylated at serine 139

PFGE: Pulse field gel electrophoresis

LET: Linear energy transfer (typical unit: keV/µm)

## ABSTRACT

**Background:** Several proteins involved in the response to DNA double strand breaks (DSB) form microscopically visible nuclear domains, or foci, after exposure to ionizing radiation. Radiation-induced foci (RIF) are believed to be located where DNA damage is induced. To test this assumption, we analyzed the spatial distribution of 53BP1, phosphorylated ATM and γH2AX RIF in cells irradiated with high linear energy transfer (LET) radiation.

**Methodology/Principal Findings:** Since energy is randomly deposited along high-LET particle paths, RIF along these paths should also be randomly distributed. The probability to induce DSB can be derived from DNA fragment data measured experimentally by pulsed-field gel electrophoresis. We used this probability in Monte Carlo simulations to predict DSB locations in synthetic nuclei geometrically described by a complete set of human chromosomes, taking into account microscope optics from real experiments. As expected, simulations produced DNA-weighted random (Poisson) distributions. In contrast, the distributions of RIF obtained as early as 5 min after exposure to high LET (1 GeV/amu Fe) were non-random. This deviation from the expected DNA-weighted random pattern can be further characterized by "relative DNA image measurements". This novel imaging approach shows that RIF were located preferentially at the interface between high and low DNA density regions, and were more frequent in regions with lower density DNA than predicted. This deviation from random behavior was more pronounced within the first 5 min following irradiation for phosphorylated ATM RIF, while γH2AX and 53BP1 RIF showed very pronounced deviation up to 30 min after exposure.

**Conclusions/Significance:** These data suggest the existence of repair centers in mammalian epithelial cells. These centers would be nuclear sub-domains where DNA lesions would be collected for more efficient repair.

## INTRODUCTION

DNA damage induced by ionizing radiation (IR) elicits formation of microscopically visible nuclear domains (i.e. foci) marked by recruitment of certain protein (e.g. 53BP1) or by particular modifications such as histone phosphorylation (γ–H2AX) or as a result of both (e.g. phosphorylated ATM, ATMp) [1-10]. Radiation-induced foci (RIF) are believed to form at or near sites of DNA damage. However, the use of RIF as an unequivocal indicator of double strand break (DSB) is problematic. The readout of RIF is complex as it is based on the optical limitation during image acquisition (e.g. point spread function), non-homogeneity of the detector and biological kinetics. Other research groups and the one presenting this work have suggested that the frequency of RIF probably reflects several factors: (1) the chromatin location of damage, (2) the severity of the damage, (3) the efficiency of damage recognition, (4) repair capacity, and (5) the biological function of the specific RIF proteins [7,11-14]. Furthermore, some reports suggest that there may be nuclear regions that are excluded from forming RIF. More specifically, in studies using densely ionizing particles that would lead to continuous DSB along their trajectories, nuclei showed discontinuous MRE11 RIF, with large gaps (> 1 μm) in regions where DNA was present [15].

How can one then sort out and interpret results on RIF formation to understand better repair mechanisms? One way to answer this question is to test through computer modeling the similarity of DNA damage patterns between real cells exposed to different radiation qualities and simulated theoretical patterns. Different radiation qualities lead to different spatial distributions of energy deposition in a volume (e.g. low *vs.* high LET, sparsely *vs*. densely ionizing radiation). Two types of radiation were used in this study, gamma-rays and high energy particles (HZE), creating very distinct DNA damage spatial pattern. HZE deposits its energy in a random clusters along a linear path [16,17]. Cells exposed to HZE are thus ideal to study the relationships between chromatin patterns and energy deposition since it reduces analysis to one-dimensional linear profiles. In contrast, gamma-rays deposit their energy uniformly at a given depth and thus induce single DSB randomly scattered across the nucleus. Relating these damages to chromatin patterns is more complex in this case since it requires three-dimensional image analysis.

Spatial patterns of radiation-induced DSB for a given DNA structure can be predicted solely on the basis of well-accepted knowledge of physical interaction of radiation with matter [18]. By using computational models that simulate the production of DSB in hypothetical spatial geometries [19,20], one could refine chromosome compartmentalization to include higher order structures such as euchromatin and heterochromatin. In addition, we have previously shown that DSB can be generated as a stochastic process with parameters determined by fitting data from DNA fragments sizes measured in pulsed-field gel electrophoresis experiments [21-23]. We thus introduce an approach that uses these tools to generate artificial microscope images of nuclei exposed to radiation. Optical limitations of light microscopy as well as DNA heterogeneity are also taken into account in the model. DSB data processed that way lead to images with foci-like objects referred as pseudo-RIF (i.e. pRIF).

Such approach permitted to test the controversial equivalence between RIF and DSB. If RIF were in fact DSB observed at a much lower resolution, then pRIF and RIF should have similar spatial distribution and frequencies. Briefly, our results showed that within 5 to 30 minutes following exposure to high- and low-LET radiation, RIF positions gradually deviated from their predicted random pattern and relocated into self-excluding nuclear sub-domains. This kinetic process suggests that physical parameters of DNA organization and physical locations of RIF influence and perhaps hinder the repair of DNA damage.

## RESULTS

### Generation of pseudo RIF (pRIF) in synthetic nuclear images

In this approach, the three-dimensional space was divided into cubic pixels of the size equals to that of microscopy image pixels (i.e. 0.16 μm). DNA in the simulated nucleus was arranged into two types of intermittent bands: dense regions of DNA based on random-walk geometry (heterochromatin), and low-density homogenous regions (euchromatin). DNA double strand breaks (DSB) were simulated by Monte Carlo simulations for single traversal of 1 GeV/amu Fe ions or for exposure to 1 Gy of X-ray [24]. Theoretical DSB are absolute whereas the visualization, and quantitation, of RIF is subject to optical limitations during image acquisition. To more closely approximate RIF from theoretical DSB, DSB were blurred by applying a Gaussian filter with $\sigma$=0.16 μm, determined by the point-spread function of the microscope, to create more realistic images. These model images of the nuclear density were similar to the experimental images of human cells stained for DAPI and generated nuclear images (see Figure 1). Applying the Gaussian blurring (Gaussian convolution) to the DSB frequency image produced images with foci-like objects, which we refer to as pseudo-foci (pRIF) and which reflects the appearance of DSB at such resolution should they emit enough fluorescence to be detected.

### Comparing pRIF frequencies and experimental RIF frequencies

To validate whether the frequency of theoretical pRIF, determined from synthetic nuclei, is comparable to actual measurements, the frequency of RIF was measured for different DNA damage markers (53BP1, γH2AX and ATMp) and for low- and high-LET radiation within the first hour following exposure to 1 Gy. The measured frequencies are shown in Table 1. For high LET radiation, we obtained excellent agreement between pseudo- and measured RIF, leading to a maximum of 0.73 RIF/μm 4.5 min following exposure to 1 GeV/amu Fe. On the other hand, consistent with our previous findings and those of others [7,11-15], measured frequencies for RIF in three-dimensional volume following low-LET do not match at all the predicted values, with a 40% loss in real data compared to pRIF.

Table 1 also shows the effect of the point-spread function (see method) on visualizing DSB by light microscopy. For low-LET simulations, there is little variance between predicted DSB and pRIF. A 1:1 correspondence between DSB and pRIF is expected for low-LET as individual DSB remains separate after optical blurring for such sparse damage events. On the other hand, for high-LET radiation, the frequency of pRIF and DSB, both generated from synthetic nuclear images, differed by 30%. The 30% loss between DSB and pRIF was due to clustering of DSB within areas that are not resolvable by light microscopy.

Therefore, these results suggest that RIF induced by high-LET radiation represent some DSB clustering observed at a lower resolution compared to the original scale of DNA breaks (nm versus μm). Interestingly, this also suggests that if a damage is severe enough (i.e. cluster of DSBs) it will most likely induce RIF, whereas single DSB do not always lead to RIF.

Table 1 RIF frequencies in experimental data and simulations for high- and low-LET radiation.

| | Marker | 1 GeV/amu Fe (foci/μm) (4.5 min post IR)* | 1 Gy of Cs (foci/nucleus) (30-60 min post IR)† |
|---|---|---|---|
| **Experimental microscope measurements** | **γH2AX** | 0.69 +/- 0.03* | 15.9 +/- 0.5† |
| | **ATMp** | 0.82 +/- 0.05* | 16.0 +/- 1.9† |
| | **53BP1** | 0.76 +/- 0.03* | 16.3 +/- 0.6† |
| **Simulations** | **DSB** | 1.10 +/- 0.48‡ | 38.1 +/- 5.9‡ |
| | **pRIF** | 0.73 +/- 0.22‡ | 37.0 +/- 5.5‡ |

**Use of an imaging approach to predict DSB location in real images**

pRIF predictions presented previously are based on DNA patterns from hypothetical nuclei, modeled at the nm scale. As described in methods, generation of DSB is dependent on DNA density. As such, any given nucleus has a unique DNA imaging pattern and a unique set of spatial probability for radiation-induced DSB. Therefore, we cannot rely on our synthetic nuclear model and pRIF imaging properties to evaluate RIF patterns measured in real images. We thus need to create an imaging methodology that would predict DSB location for any given DNA nuclear pattern from real images.

* The highest frequency for foci along tracks was measured within the first 5 min following exposure to radiation. Standard errors are based on 3 to 5 independent experiments with about 100 to 200 nuclei per experiment. Standard errors was computed as the standard deviation between the mean obtained in each experiment and normalized by the square root of the number of independents experiment.

† The highest frequency for foci after Cs exposure was measured 30 to 60 min following exposure to radiation. Standard errors are based on 2 individual time points. All counts were made in 3D (i.e. full nucleus).

‡ These values are standard deviations based on 197 and 81 synthetic nuclei for Fe and Cs respectively.

We propose to apply the same Monte Carlo concepts described in method for the generation of DSB in artificial nuclei to generate theoretical DSB imaging pattern in real nuclear images. This will be done by assuming that it remains true that the probability to generate DSB is proportional to DNA density at lower resolutions (i.e. light microscopy).

We illustrate this concept using high-LET radiation data, where tracks demarcate nicely in individual nuclei regions where damages have occurred. Within these tracks of damages, spatial 1-D profile of DNA density and the number of foci (*Nspot)* are determined (see Figure 2). Our imaging approach assumes that the probability of having a focus as a function of DNA density is given by:

$$\Pr oba = \frac{Nspot}{\sum_{Track} DNA(i)} \quad (1)$$

where *DNA(i)* is the DNA density at position *i* along the indexed pixel of the track. The probability $P_{DSB}$ of a DSB at any give pixel location along the track is then:

$$P_{DSB} = DNA(i) \times \Pr oba \quad (2)$$

If this probability is greater than a random value taken between 0 and 1, then a focus is generated at this location. Applying this approach to all the pixels along the track, we generate a set of new focus locations referred as reshuffled foci (see Figure 2).

The validity of this image methodology can be tested on the set of 197 simulated images used to generate Table 1 for exposure to 1 GeV/amu Fe. Imaging pattern of damage for such radiation can be characterized by measuring the distribution of distances between consecutive damages along tracks. We can then compare spatial patterns between pRIF and reshuffled foci by computing the correlation between their distance distributions. Figure 3 shows a very high correlation (0.95), indicating that reshuffling pRIF predicts well the actual damage distribution at such resolution. One can also note in the reshuffled pRIF distribution that even though the main shape of the pRIF distribution is conserved, higher frequency variations are not. To illustrate the effect of the PSF, distance distribution of consecutive DSBs is also shown. As expected from physical laws, this distribution follows more the expected Poisson shape with some variation due to the inability to resolve distance less than 0.16 um and the lack of uniformity of DNA along the track.

This therefore strongly suggests that the *probability of generating DSB remains proportional to DNA density at a lower resolution (i.e. sub-micron*) and validates our imaging approach to predict DSB pattern in real images.

**Reshuffling experimental RIF to predict DNA damage pattern for a given nucleus**

As we validated *in silico* our imaging approach to predict DNA damage patterns along HZE track, we next compare actual RIF with predicted RIF *in situ* for the same radiation quality. DAPI is a typical nuclear dye. It is known to bind to AT base pairs or to single strands by electrostatic interaction. Therefore, one can assume as a first order approximation that the pixel intensity in a DAPI image is proportional to the DNA concentration at that location. We will therefore use DAPI as an indicator of DNA densities in real images and ATMp, γH2AX and 53BP1 as different DNA damage markers.

Using such labels on cells irradiated by 1 GeV/amu Fe, our results indicate that the distribution of foci along tracks deviates from truly random distribution. This deviation increases with time independently of the marker used for damage. This is illustrated in Figure 4 for γH2AX, where the distance distribution between consecutive foci is compared to the distribution of reshuffled γH2AX foci at 4.5 and 30 min following exposure to 1 GeV/amu Fe. As early as 4.5 min post-IR, only 60% of distribution correlates with the expected distance distribution of predicted damages (i.e. reshuffled RIF) and this lack of correlation increases with time. One can also notice that the most significant difference between the predicted behavior and the measured RIF is the absence of foci less than 1 μm apart. This exclusion phenomenon seems to increase with time. Figure 5A summarizes these results for all the time points we considered (4.5, 11.5, 31.5, 61.5 min) by plotting the average correlations measured between predicted (i.e. reshuffled foci) and measured distance distribution for the different DNA damage labels we have been using in this work. All labels show the same trend with an increasing deviation from random distribution over the first hour following exposure to 1 Gy of 1 GeV/amu Fe. Note that the predicted RIF distance distribution is based on reshuffling the exact same number of detected RIF for each individual analyzed track. Therefore, the stronger deviation from randomness at later time point cannot be attributed to a larger average spacing due to a decreasing number of foci along the tracks as shown in Figure 5B. In fact, *this increasing deviation from randomness is indicative of a rapid movement of DNA damage into self-excluding sub-regions of the nucleus within an hour following exposure to HZE.*

**Relative DNA image measurements**

Distance distribution is an interesting parameter to monitor the organization of damage in the nucleus and determine the deviation from randomness with time. However, distance distribution does not identify where the foci relocate with respect to nuclear regions. To do so, we established a set of imaging parameters that reflects the position of foci with respect to DNA density. This set of parameters can also be measured in any spatial dimensions (i.e. line profiles, surfaces or volumes). Figure 6 illustrates the approach for different foci pattern for a given nucleus (i.e. center slice of a nucleus - DAPI stain). Using automatic spot detection (see method), we consider the center of RIF as the brightest pixel in its vicinity. One can then compute the mean DNA density signal at the centers of all RIF in one nucleus and normalize it to the mean nuclear DNA density to get a relative DNA density value at these locations. We thus define the relative density of DNA at the foci locations as follows:

$$Rdna = \frac{\sum_{i=focus} I(i) \Big/ N_{focus}}{\sum_{i=nucleus} I(i) \Big/ N_{nucleus}} \quad (3)$$

where, *I(i)* is the intensity at pixel location *i*, $N_{focus}$ is the number of foci and $N_{nucleus}$ is the number of pixel in the nucleus (note, *i=focus* refers to the brightest pixel in an identified focus). Since foci formation probability is proportional to DNA content, we expect to see *Rdna* larger than 1.

We *hypothesize that proximal regions to high chromatin compaction may be important regions for DNA repair* and thus want to evaluate the relative position of foci to such regions. Therefore we investigated RIF positioning in relation to the relative DNA gradient, *Rgrad* as described in Figure 6. The DNA gradient is a good indicator of edges between high and low DNA density region. Similarly to *Rdna* definition, *Rgrad* is the mean DNA gradient at the foci location normalized to the mean gradient over the full nucleus, defined as follow:

$$Rgrad = \frac{\sum_{i=focus} \nabla I(i) \Big/ N_{focus}}{\sum_{i=nucleus} \nabla I(i) \Big/ N_{nucleus}} \quad (4)$$

where, $\nabla I(i)$ is the Euclidian norm of the gradient vector of *I(i)* at pixel location *i*.

**Note that we used a conservative segmentation of the nucleus, so that the contour defining the nucleus was 3 pixels** (i.e. 0.48 μm) inward of the boundary of the nucleus removing any edge effect when computing the gradient of the nuclear DAPI image (see Figure 6).

Now that we have defined "relative DNA image measurements", let us apply it to pRIFs in simulated 1 GeV/amu Fe tracks. As we had expected, *Rdna* values for pRIF are greater than one (see Table 2 below). On the other hand, *Rgrad* values are also larger than one for pRIF. This result at first hand might look surprising as one would assume that there should be no preferential location of DSB at the interface between high and low DNA density regions in the simulation. However, a value higher than one is in fact due to a bias of the gradient towards higher values since pRIFs occur preferentially in the brighter regions of DNA.

*Rdna* and *Rgrad* values are highly dependent on the DNA pattern in the nucleus with larger DNA density variations in the nucleus leading to higher *Rdna* values. Therefore, in order to interpret *Rdna* and *Rgrad* values in real experimental images, we need to have a way to know what to expect. By using the reshuffling method we previously introduced

to predict normal DSB pattern at the imaging level, we can determine the expected *Rdna* and *Rgrad* values. When doing so on synthetic data, we find that *Rdna* and *Rgrad* values for reshuffled pRIFs are extremely similar to the ones determined for pRIF (see Table 2). This further validates our imaging approach for predicting DSB pattern. In addition, by reporting the ratio of *Rdna* and *Rgrad* values with the corresponding values generated from reshuffled foci (i.e. *R1/R2* and *Rg1/Rg2*, last column in Table 2), one can then report a normalized value independent of nuclear pattern variation. A ratio of 1 would indicate a foci pattern that matches the expected random pattern of DNA damage.

Table 2 – Reshuffling simulated foci positions along synthetic tracks lead to the same relative DNA values than simulations.

| | **pRIF(1)*** | **Reshuffled pRIF (2)*** | **Ratio (1)/(2)*** |
|---|---|---|---|
| **Rdna (R)** | 1.10 +/- 0.10 | 1.12 +/- 0.07 | **0.98 +/- 0.07** |
| **Rgrad (Rg)** | 1.09 +/- 0.26 | 1.1 +/- 0.09 | **0.99 +/- 0.26** |

While prediction of frequencies of RIF following low-LET IR is problematic (see Table 1), our spatial analysis of RIF position can thus be generalized for sparsely ionizing radiation (i.e. X-rays). We first validated this approach *in silico* on three-dimensional synthetic nuclei exposed to 1 Gy of X-ray, as done previously for Fe tracks (i.e. Table 2 and Figure 3). A set of 80 simulated nuclei exposed to X-rays (see Figure 1B for example of X-rays simulation) were analyzed by automatically identifying pRIF positions to compute theoretical *Rdna* and *Rgrad* values. These values were also compared to relative DNA measurements made for reshuffled pRIF in each 3D nucleus. Reshuffling was done in the same manner it was done for 1D profile, by using DNA density as a probability to have damage. This led to ratios closed to 1 (i.e. *R1/R2* equal to 1.05 +/- 0.09 and *Rg1/Rg2* of 0.96 +/- 0.11). Therefore, one can predict, based upon a randomized distribution, the imaging pattern of DSB when observed at the resolution of light microscopy by simply assuming that the probability of a focus being at a given location will be proportional to the DNA density at that location. In other words, we just proved using synthetic images and computer models that one can compare *Rdna* and *Rgrad* values of RIF in any irradiated nucleus with the expected value of pRIF for the same nucleus by reshuffling RIF position in the nucleus using the DAPI image as a probability function.

**Relative DNA measurements applied to the experimental data**

We first applied relative DNA measurements to high LET track data (i.e. 1D profiles). The 95% confidence intervals for the predicted ratios, based upon a random distribution determined by DNA content, are shown in Fig. 7A,B,C. *Rdna* and *Rgrad* measurements along tracks shown in Figure 7A,B,C confirm a deviation of RIF spatial distribution from

* Standard errors are based on 3 to 5 individual experiments with about 100 to 200 nuclei per experiment as defined in Table 1.

the predicted damage nuclear location within the first 35 min following exposure to 1 GeV/amu Fe. During that time period, *Rdna* averages are always less than 1 for any time point, as early as 4.5 min post-irradiation and *Rgrad* averages are always above 1. This indicates that on average, RIF locate themselves in lower DNA density region than where DSBs are expected to occur, and RIF tend to be preferably located at the interface between high and low DNA density regions (see Figures 7DEF for illustration of phenomenon). Interestingly, while γH2AX and 53BP1 foci deviate significantly from the predicted ratios during the first 35 minutes following irradiation, ATMp foci show a slightly different dynamic. At the earliest time point post-IR, ATMp containing foci localize to chromatin regions of slightly less DNA at the interphase of high and low densities. However by 10 minutes post-IR, these foci, on average, have relocalized.

The application of this analysis to gamma-rays data requires a few careful imaging considerations. For instance, due to the poor resolution of a conventional microscope image in the Z direction, *Rdna* and *Rgrad* computations were only done in 2D, using the best focal plane of 3D stacks of each cell (see Figure 8). Also, as mentioned earlier (Figure 6), a more limited segmentation of the nucleus need be used to avoid the high gradient values of the nuclear edges. Our results show that *Rdna* values are all very close but smaller than 1 for all three DNA damage markers as summarized in Table 3. On the other hand, one can also note the robustness of such measurements with very small standard errors (i.e. relative standard errors between 0.3% and 2%), allowing us to detect very subtle differences and showing statistical significance of these lower values for γH2AX early after exposure to radiation. As also shown for track data, RIF for all markers tend to locate themselves preferentially at the interface between high and low DNA densities (i.e. *Rgrad* higher than 1). These features are further illustrated in Figure 8, showing a representative nucleus for this analysis.

Table 3 – Experimental relative DNA measurements normalized to predicted for exposure for 1 Gy of gamma-rays

| **Ratio: Measured/predicted** | **Time post IR (min)** | **γH2AX[*] (n=3)** | **53BP1[*] (n=6)** | **ATMp[*] (n=3)** |
|---|---|---|---|---|
| **Rdna** | 4.5 | **0.98 +/- 0.008**[†] | 0.98 +/- 0.001 | 0.97 +/- 0.006 |
| | 10-60 | 1.00+/- 0.01 | 0.99 +/- 0.003 | 0.98 +/- 0.01 |
| **Rgrad** | 4.5 | **1.06 +/- 0.003**[†] | **1.04 +/- 0.02**[†] | 1.04 +/- 0.02 |
| | 10-60 | 1.02 +/- 0.01 | **1.01 +/- 0.007**[†] | 1.01 +/- 0.01 |

[*] Standard errors are based on replicate experiments on same batch of cells (number of replicates indicated by variable *n*)

[†] Measured values are significantly different from predicted values based on T-test (i.e. ratio significantly different from 1)

**Increase co-localization of DNA damage markers over the first 10 min following exposure to radiation**

In order to test if DNA damage markers shift position after exposure to radiation, we quantified the amount of co-localization of γH2AX and ATMp to the same DNA damage marker, i.e. 53BP1 (Figure 9). Both markers showed the same pronounce response of a quick increase of co-localization to 53BP1, independently of the radiation quality. This increase was statistically significant for cells exposed to 1 Gy of 1 GeV/amu Fe, with an increase from 44% to 64% of co-localization within the first 10 min following radiation. Representative images are shown in Figure 9B. It is important to note here that for both high- and low-LET, changes for foci frequency within this time period was limited (i.e. 2 to 7%, all labels included). Therefore, a 20% increase of co-localization cannot be explained by foci appearing or disappearing over this period of time, but instead suggests relocalization of one, or both markers to a common region of the nucleus.

## DISCUSSION

RIF can be considered as biological indicators of localized DNA damage. Comparing predicted initial spatial pattern of DNA damage in a nucleus to its actual damage pattern suggests that DSB lead to a rapid reorganization of the nucleus. Monte Carlo simulations show that the initial distribution of pRIF along the direction of a track should be truly random (Poisson distributed in a given interval along a track). Of course, this is not true for the direction perpendicular to the track, where pRIF are severely clustered and prone to produce streaks of DSB, as determined by the track geometry. However, in contrast to the model, the distribution of RIF along a track, at our earliest time point (4.5 min), already shows some regularity in their spatial distribution. For instance, within the first 30 min following exposure to 1 GeV/amu Fe, foci distribution along the tracks go from 60% to 45% in agreement with prediction, suggesting either movement of RIF in the nucleus or chromatin reorganization (Fig. 5A). This loss of correlation takes into account the lower frequency of foci at 30 min (Fig. 5B) and can be attributed entirely to an exclusion of foci in close proximity. This can be interpreted as either a clustering of DNA damage into specific sub-domains of the nucleus or a more global remodeling of the nuclear architecture after irradiation as suggested by others [25,26].

To understand better the involvement of chromatin, we introduce a new set of imaging parameters that correlate foci positions to nuclear density and its gradient. By doing so, we show that RIF are more frequently located in low DNA density regions than predicted by modeling and occur predominantly at the interface between high and low DNA density regions (Fig. 7). In addition, we show a rapid increase of co-localization of different DNA damage markers over the first 10 min following exposure to radiation, suggesting a clustering process of these different markers to a common sub-domain of the nucleus. Interestingly, ATMp is the only DNA damage marker that fails to have any of these significant trends (except for time points less than 5 min post-IR). This finding reveals the quantitative power of our approach by confirming that ATMp is upstream of

53BP1 and γH2AX in the repair pathway, and only serves a brief role in the assembly of repair complex. Once ATMp has served its role in RIF formation, it returns to a random pattern as the one expected from the initial DSB pattern before being dephosphorylated.

In the light of this work, we hypothesize that the type of chromatin organization where DSB are generated dictates the kinetics of RIF formation and therefore influences DNA repair. More specifically, breaks occurring in more condensed regions of DNA may need either local decondensation of chromatin as suggested by others [25,26] or DSB relocation to more open regions of the chromatin in order to start the repair process. DNA damage marker would then not be detected until they would be revealed to more open regions of the nucleus. One strong argument in favor of DSB movement instead of local decondensation is the rapid accumulation of repair proteins at the interface between high and low DNA density that we are reporting in our work and that has no physical basis. In addition, no obvious chromatin decondensation after exposure to radiation has been apparent when imaging live cells labeled with nuclear dies (data not shown). Finally, this is not such a surprising hypothesis as similar phenomena have been observed for transcription, where a gene becomes active only when relocating into an open region of the nucleus [27], with the possibility of some part of the chromosome moving over a 1 to 5 μm path within a few minutes in mammalian cells [28]. In fact, one group hypothesized some time ago that Ku proteins might recruit DSB to DNA-PKcs (catalytic subunit of DNA-PK) which is fixed on the nuclear matrix, allowing fast DNA repair via nonhomologous end-joining (NHEJ) [29]. More recently, it was shown that MRN complex "tethers" damaged DNA to help activate ATM by increasing locally the concentration of DSBs [30]. In conclusion, our data may suggest the existence of repair centers in mammalian epithelial cells as it has been shown in yeast [31]. These repair centers would be nuclear sub-domains where DNA lesions could be repair more efficiently and rapidly via NHEJ. However, the DNA damage response involves many players and many different nuclear sub-domains [32] and our interpretation probably reflects only one of many nuclear sub-domains involved in repair.

## MATERIAL AND METHODS

**Cell culture:** Human mammary epithelial cells (HMEC-184; 184v; passage 7-10) were cultured in serum free medium as previously described [33]. HMEC-184 were irradiated with 1 Gy of ionizing radiation 2 days post-plating. We used a 5600 curie source of 137-Cs for γ-radiation and 1 GeV/amu Fe ions from the NASA Space Radiation Laboratory of the Brookhaven National Laboratory.

**Reagents:** Primary: mouse monoclonal anti phospho-histone H2AX (Ser139) antibody (Lot # 27505; Upstate Cell Signaling Solutions Inc. Charlottesville, VA) used at 1.42 μg/ml; mouse monoclonal anti phosphorylated (pS1981) ATM protein kinase antibody (Lot # 14354; Rockland Inc., Gilbertsville, PA) used at 2.15 μg/ml; rabbit polyclonal anti 53BP1 (Lot # A300-272A, Bethyl Lab, Montgomery, TX) used at 5 μg/ml; All

secondaries were used at 1:300 (Dk anti Rb Alexa 594, Lot# 40247A, and Gt anti Ms Alexa 488 , lot A11029 from Molecular Probes, Invitrogen, Carlsbad, CA).

**Immunofluorescence:** Cells were grown on tissue culture treated LabTek 8-well chamber slides. Chambers were fixed at room temperature for 15 min using 2% paraformaldehyde followed by successive wash and permeabilization with 100% Methanol for 20 min at -20$^{o}$C. Non-specific sites were blocked using 1% BSA for 90 minutes. The cells were incubated two hours at room temperature with primary antibodies in blocking buffer in a humidified chamber. Following washes, primary antibody binding was detected using species appropriate fluorochrome labeled secondary antibodies (Molecular Probes) incubating for 1 hour at room temperature. Nuclei were counterstained with DAPI (4',6-Diamidino-2-Phenylindole) using 0.5 μg/ml. Slides were mounted in Vectashield (Vector Laboratories Inc., Burlingame, CA) and stored at -20°C until evaluated.

**Image analysis:** Cells were viewed and imaged using a Zeiss Axiovert epifluorescence microscope (Carl Zeiss, Jena, Germany) equipped with a multiband pass filter and a differential wavelength filter wheel. Images were acquired using a Zeiss plan-apochromat 40X dry, with a NA of 0.95 and a scientific-grade 12-bit charged coupled device camera (ORCA AG Hamamatsu, 6.45 x 6.45 μm$^2$ pixels). The image pixel size was measured to be 0.16 μm but based on the NA of the objective, the actual resolution of the image in the FITC channel is ~ 0.5x0.488/NA = 0.26 μm. All images were captured with the same exposure time so that intensities were within the 12-bit linear range. All image manipulation and analysis were done with Matlab (MathWorks, Inc., Natick, MA) and DIPimage (image processing toolbox for Matlab, Delft University of Technology, The Netherlands). For track analysis, Fe ion tracks were manually identified on the-most-in-focus-slice in a conventional image stack, by drawing a line along the track. Such line was recorded as a track, only if it had 4 or more foci, and if the cells on the stack slice had parallel tracks, reinforcing the assertion that the line in question was the result of a particle traversal and not a simple random alignment of points (see Figure 2). To keep track of the radial (perpendicular to the track) displacement of foci, the image stripe of 0.8 μm across was sampled for the maximum intensity in the direction perpendicular to the track to produce a one-dimensional function of maximal intensities along the track. Herein this function will be called the “maximum intensity profile”, or simply the “1D profile” (Figure 3). Using the 1D profile, foci were detected by searching for local maxima and minima along the track as shown on the image (Figure 3). This was done by detecting the local maxima on the original image, and the local minima on intensity-inverted image using watershed algorithms. For foci detection in cells exposed to gamma-rays, The tophat algorithm was first applied to the image (or tophat convolution). This algorithm would enhance maxima with a spherical shape. This convolution was followed by the watershed algorithm to determine the local maxima and minima along the 1D profile. In both 1- and 3-D cases, the center of the RIF was determined as a pixel with the maximum intensity as sampled over the identified RIF. These central pixels were taken as RIF coordinates and utilized for Rdna and Rgrad computations (defined below), and for co-localization analysis. More details on the methods of image processing and analysis are in Results.

**Generation of DSB by Monte Carlo Technique in virtual nuclei**

The Monte Carlo algorithm utilized here is based on the fact that the probability to have a DNA double strand break at a given location in the nucleus is proportional to the DNA density and the dose (energy per unit mass) deposited at that location. As shown previously [22,24] the spatial DSB distribution is generated via a stochastic process given by

$$\psi = 1 - \exp(-QD(t)) \quad (5)$$

where $\psi$ is a probability to create a DSB at a monomer (a small stretch of DNA containing 2 kbp of genomic information), $D(t)$ is the local dose given by the track structure (it can vary sharply with the distance $t$ from the track center), and $Q$ is the constant determined from model fits to Pulsed-Field Gel Electrophoresis (PFGE) data. The correctly determined $Q$ would generate proper DSB yields, fragment-size distribution functions, average numbers of DSB per nucleus per track, and the spatial distributions of DSB [19,22] for several ions, any $E$, and any dose. In this approach the frequency of DSB would depend on the properties of a track given by $D(t)$ [18,34], but it will also depend on the DNA configuration given by a random walk model, as the probability $\psi$ is applied to each monomer. In this model a pixel can have a variable number of monomers corresponding to the density fluctuations of genetic material in the nucleus with high precision.

## ACKNOWLEDGEMENTS

The authors would like to thank Dr. Christopher A. Maxwell for his critical review of the manuscript and Mr. William Chou for technical support. This research was supported by National Aeronautics and Space Administration Grant no. T6275W, NASA Specialized Center for Research in Radiation Health Effects.

## REFERENCES

1. Rogakou EP, Pilch DR, Orr AH, Ivanova VS, Bonner WM (1998) DNA double-stranded breaks induce histone H2AX phosphorylation on serine 139. J Biol Chem 273: 5858-5868.
2. Paull TT, Rogakou EP, Yamazaki V, Kirchgessner CU, Gellert M, et al. (2000) A critical role for histone H2AX in recruitment of repair factors to nuclear foci after DNA damage. Curr Biol 10: 886-895.
3. Celeste A, Petersen S, Romanienko PJ, Fernandez-Capetillo O, Chen HT, et al. (2002) Genomic instability in mice lacking histone H2AX. Science 296: 922-927.
4. MacPhail SH, Banath JP, Yu TY, Chu EH, Lambur H, et al. (2003) Expression of phosphorylated histone H2AX in cultured cell lines following exposure to X-rays. Int J Radiat Biol 79: 351-358.
5. Kurz EU, Lees-Miller SP (2004) DNA damage-induced activation of ATM and ATM-dependent signaling pathways. DNA Repair (Amst) 3: 889-900.

6. Balajee AS, Geard CR (2004) Replication protein A and gamma-H2AX foci assembly is triggered by cellular response to DNA double-strand breaks. Exp Cell Res 300: 320-334.
7. Karlsson KH, Stenerlow B (2004) Focus formation of DNA repair proteins in normal and repair-deficient cells irradiated with high-LET ions. Radiat Res 161: 517-527.
8. Anderson L, Henderson C, Adachi Y (2001) Phosphorylation and rapid relocalization of 53BP1 to nuclear foci upon DNA damage. Molecular and Cellular Biology 21: 1719-1729.
9. Rappold I, Iwabuchi K, Date T, Chen J (2001) Tumor suppressor p53 binding protein 1 (53BP1) is involved in DNA damage-signaling pathways. J Cell Biol 153: 613-620.
10. Schultz LB, Chehab NH, Malikzay A, Halazonetis TD (2000) p53 binding protein 1 (53BP1) is an early participant in the cellular response to DNA double-strand breaks. J Cell Biol 151: 1381-1390.
11. Costes SV, Boissiere A, Ravani SA, Romano R, Parvin B, et al. (2006) Imaging features that discriminate between high and low LET radiation-induced foci in human fibroblasts. Radiat Res 165: 505-515.
12. Han J, Hendzel MJ, Allalunis-Turner J (2006) Quantitative analysis reveals asynchronous and more than DSB-associated histone H2AX phosphorylation after exposure to ionizing radiation. Radiat Res 165: 283-292.
13. Reitsema TJ, Banath JP, MacPhail SH, Olive PL (2004) Hypertonic saline enhances expression of phosphorylated histone H2AX after irradiation. Radiat Res 161: 402-408.
14. MacPhail SH, Banath JP, Yu Y, Chu E, Olive PL (2003) Cell cycle-dependent expression of phosphorylated histone H2AX: reduced expression in unirradiated but not X-irradiated G1-phase cells. Radiat Res 159: 759-767.
15. Jakob B, Scholz M, Taucher-Scholz G (2003) Biological imaging of heavy charged-particle tracks. Radiat Res 159: 676-684.
16. Magee JL, Chatterjee A (1980) Radiation chemistry of heavy-particle tracks. 1. General considerations. J Phys Chem 84: 3529-3536.
17. Zeiss GD, J. MW, F. MJC, J. DD (1975) Dipole spectrum of water vapor and its relation to the energy loss of fast-charged particles. Rad Res 63: 64-82.
18. Cucinotta FA, Nikjoo H, Goodhead DT (1999) Applications of Amorphous Track Models in Radiation Biology. Radiat Environ Biophys 38: 81-92.
19. Ponomarev AL, Cucinotta FA (2006) Chromatin loops are responsible for higher counts of small DNA fragments induced by high-LET radiation, while chromosomal domains do not affect the fragment sizes. Int J Radiat Biol 82: 293-305.
20. Munkel C, Eils R, Dietzel S, Zink D, Mehring C, et al. (1999) Compartmentalization of interphase chromosomes observed in simulation and experiment. J Mol Biol 285: 1053-1065.
21. Sachs RK, Ponomarev AL, Hahnfeldt P, Hlatky LR (1999) Locations of radiation-produced DNA double strand breaks along chromosomes: a stochastic cluster process formalism. Math Biosci 159: 165-187.

22. Ponomarev AL, Cucinotta FA, Sachs RK, Brenner DJ, Peterson LE (2001) Extrapolation of the dna fragment-size distribution after high-dose irradiation to predict effects at low doses. Radiat Res 156: 594-597.
23. Ponomarev AL, Brenner D, Hlatky LR, Sachs RK (2000) A polymer, random walk model for the size-distribution of large DNA fragments after high linear energy transfer radiation. Radiat Environ Biophys 39: 111-120.
24. Ponomarev AL, Cucinotta FA (2006) Novel image processing interface to relate DSB spatial distribution from experiments with phosphorylation foci to the state-of-the-art models of DNA breakage. Radiation Measurements, Space Radiation Transport, Shielding, and Risk Assessment Models 41: 1075-1079.
25. Bakkenist CJ, Kastan MB (2003) DNA damage activates ATM through intermolecular autophosphorylation and dimer dissociation. Nature 421.
26. Kruhlak MJ, Celeste A, Dellaire G, Fernandez-Capetillo O, Muller WG, et al. (2006) Changes in chromatin structure and mobility in living cells at sites of DNA double-strand breaks
10.1083/jcb.200510015. J Cell Biol 172: 823-834.
27. Cremer T, Cremer C (2001) Chromosome territories, nuclear architecture and gene regulation in mammalian cells. Nat Rev Genet 2: 292-301.
28. Chuang CH, Carpenter AE, Fuchsova B, Johnson T, de Lanerolle P, et al. (2006) Long-range directional movement of an interphase chromosome site. Curr Biol 16: 825-831.
29. DiBiase SJ, Zeng ZC, Chen R, Hyslop T, Curran WJ, Jr., et al. (2000) DNA-dependent protein kinase stimulates an independently active, nonhomologous, end-joining apparatus. Cancer Res 60: 1245-1253.
30. Dupre A, Boyer-Chatenet L, Gautier J (2006) Two-step activation of ATM by DNA and the Mre11-Rad50-Nbs1 complex. Nat Struct Mol Biol 13: 451-457.
31. Lisby M, Mortensen UH, Rothstein R (2003) Colocalization of multiple DNA double-strand breaks at a single Rad52 repair centre. Nat Cell Biol 5: 572-577.
32. Bekker-Jensen S, Lukas C, Kitagawa R, Melander F, Kastan MB, et al. (2006) Spatial organization of the mammalian genome surveillance machinery in response to DNA strand breaks
10.1083/jcb.200510130. J Cell Biol 173: 195-206.
33. Stampfer MR (1985) Isolation and growth of human mammary epithelial cells. J Tissue Culture Met 9: 107-115.
34. Cucinotta FA, Nikjoo H, Goodhead DT (2000) Model for radial dependence of frequency distributions for energy imparted in nanometer volumes from HZE particles. Radiat Res 153: 459-468.

**FIGURE LEGEND**

**Figure 1 Comparison between simulated and experimental images for different types of radiation.** Panel A shows radiation induced foci (RIF) within a nucleus traversed by high energy Fe ions (1 GeV/amu Fe) and panel B shows a nucleus exposed to photons. Shown on the left are RIF images of nuclei taken from a microscope (DAPI in blue and DNA damage marker γH2AX in green) 5 to 10 min post irradiation. On the right are pseudo RIF (pRIF) microscopic images at the same magnification. These pRIF images are generated by blurring DNA damage simulations for equivalent doses of radiation with the point spread function of the optic used. For pRIFs, the blue channel shows the resulting nuclear density and the green channel shows double strand breaks (DSBs). If the point spread function is omitted from the simulation, DSB locations can be better resolved as shown in the gray images at the right of each panel (brightness proportional to the number of breaks within each pixel).

**Figure 2 Illustration of image manipulation to predict the average DNA damage pattern along a track for a given DNA density profile.** Panel A shows a typical image of cells that have been traversed with 1 Gy of 1 GeV/amu Fe ions. After manually selecting a region that contains a clear track, foci identification and reshuffling is done as depicted by the cartoon. Foci detection is done automatically via in-house image algorithm (see method). Panel B further illustrates the mathematical approach used (i.e. Monte Carlo concept), where the probability of damage at a pixel location is proportional to the DNA density at the same location. This process is done iteratively (i.e. 50 randomization per nucleus analyzed) to give a reasonable average break distribution. For each iteration, RIF position is determined by a probability less than that determined by DNA densisty (blue line).

**Figure 3 Comparison of image prediction and Monte Carlo simulation for DNA damage distance distribution.** Panel A shows the distribution of distance between consecutive foci along the track for a set of 197 simulated nuclei exposed to a theoretical 1 GeV/amu Fe track. Panel B illustrates a simulated nucleus: DSBs are shown in red, DNA densities and DSBs blurred with the point spread function (PSF) in blue and green respectively Pseudo-RIF (pRIF, blurred DSBs) are identified by detecting maxima along the intensity profile (shown in panel C) sampled over a narrow strip of the image in Panel B. These profiles are obtained by computing the maximum intensity projection of a 0.8 μm thick line aligned with the particle track. Some of the distances reported for this illustrated track are also shown in Panel B and C and labeled correspondingly in Panel A. The average DSB distance distribution over all 197 nuclei is shown by the red dotted curve showing an expected Poisson-like distribution. The corresponding distance distribution for pRIF is shown as the dash green curve and is similar to the DSB distribution except for the frequency of close-by foci that has diminished (i.e. need at least more than 2-pixel gap to be separate, which corresponds to 0.48 μm). We could reproduce this behavior (dark solid curve) by simply randomizing pRIF along the track using the DNA profile as a probability for DNA damage (as described in Figure 2).

**Figure 4 Comparing theoretical and experimental DNA damage pattern along 1 GeV/amu Fe tracks.** Average distributions of distances between consecutive foci along Fe tracks are plotted at 4.5 min and 35 min following 1 Gy exposure (blue solid lines, panel A, B respectively). Error bars are standard errors based on 4 independent experiments. For each individual track analyzed from real data, foci were counted and their positions were then randomized based on DNA profiles, described previously, to generate a theoretical distribution pattern (red dashed lines). Measuring the correlation between theoretical and experimental distributions, we observe a decrease of correlation between these two time points, from 0.6 to 0.45. These data indicate that as early as 4.5 mins following exposure to radiation, foci positions deviate from a theoretical random behavior by 40% and this tendency increases over the next 30 mins with a 60% loss of correlation.

**Figure 5 Spatial foci pattern increasingly deviates from prediction following 1 Gy of 1 GeV/amu Fe exposure.** Panel A plots the correlation between theoretical and experimental distributions of distances between consecutive foci along Fe tracks over the first hour following exposure to radiation. All DNA damage markers used (i.e. γH2AX, ATMp, 53BP1) show the same loss of correlation to randomness over time. Panel B shows the corresponding foci frequencies, depicting a rapidly decreasing curve indicative of DNA repair. As previously described, the randomization process for prediction is applied to each analyzed experimental track and utilizes the measured frequency of foci for each track at each defined timepoint. The decrease of frequency of RIF over time is thus taken into account for predicted distance distributions. Therefore, one cannot explain the loss of correlation shown in panel A to a lower number of foci over time.

**Figure 6 Illustration of *Rdna* and *Rgrad* measurements.** Three hypothetical foci patterns over the same nucleus are illustrated with their corresponding *Rdna* and *Rgrad* values. Upper panels are overlays of the DAPI image with the center of hypothetical foci (in red). Lower panels are overlays of the foci location with the gradient image of DAPI. The gradient operator is often used in imaging as an edge detector. To illustrate this, the green arrow in panel C delineates the contour of the edge of a bright DAPI region. One can see in the corresponding gradient image in panel D that the same contour correlates to a bright gradient region. *Rdna* measures the ratio of the mean nuclear intensity at the foci locations over the mean intensity of the full nucleus. *Rgrad* measures the same ratio on the gradient image. Because the boundary of the nuclear image creates a strong gradient intensity, a conservative contour is used for nuclear segmentation (shown in blue) to avoid an edge effect when calculating *Rdna* and *Rgrad*. In images (A,B), foci are placed in areas of surrounding high nuclear density. The surrounding high density keeps the foci distal from areas of density change, thus we see the foci lie in low intensity regions in the corresponding gradient image. This results in *Rdna* above 1 and *Rgrad* below 1. By manually placing foci at different locations with respect to DNA density regions, we show that *Rdna* is high when foci are located in bright regions of the nucleus (A,B); *Rgrad* is high when foci are located at the interface of bright and dim regions of the nucleus (C,D); and *Rdna* is low when foci are located in dim regions of the nucleus (E,F).

**Figure 7 *Rdna* and *Rgrad* computation confirm rapid relocation to dim-bright nuclear interfaces with a lower proportion of foci in the high DNA density regions after exposure to 1 Gy of 1 GeV/amu Fe**

Measured *Rdna* and *Rgrad* divided by theoretical values are graphed in panel A, B and C. For all DNA marker analyzed here, all *Rgrad* ratios are above 1 and Rdna ratios are below one. This indicates a tendency of RIF to locate themselves at the interface between high and low DNA density regions and preferably in the low DNA density regions. This tendency is stronger within the first 10 min following exposure to radiation and statistically significant for gH2AX and 53BP1 for the first 30 min post-IR (significance is labeled by an asterix with the number of independent experiments in parenthesis, statistical test based on T-test between measured averages and predicted ones. Based on that test, 95% confidence interval for normal ratios is shown as gray area). For ATMp, only the earliest time point was statistically significant indicating a return to normality much faster than the other markers. A representative nucleus 3 min post-IR is shown in panel D, with γH2AX RIF appearing as green signal and DAPI shown as blue. The white dashed arrow indicates the traversal of one Fe particle and small solid color arrows indicate specific RIF. The same nucleus is seen in panel E with the DAPI intensity displayed in a three-dimensional topographic blue surface and segmented γH2AX RIF shown as green beads (Note: rendering done with Bitplane AG, Zurich, Switzerland). Panel F shows the same topographic view, sectioned along the particle trajectory to better appreciate the position of RIF with respect to the DAPI intensity profile. For orientation purposes, the same RIF shown with solid color arrows in panel D are shown in panel E and clearly illustrate the preferred location of RIF at the interface between high and low DNA density regions.

**Figure 8 Normal Human Mammary Epithelial Cell 3 min after exposure to 1 Gy of Cs.**

DAPI is shown in blue, ATMp in green and 53BP1 in red. Panel A shows a representative three-dimensional image of a nucleus in orthogonal cross-section views. The same nucleus is seen in panel B as a three-dimensional surface rendering with only DAPI and ATMp RIF being segmented (i.e blue and green surfaces respectively – rendering done with Bitplane AG, Zurich, Switzerland). This nucleus clearly shows the preferred location of ATMp RIFs at the interface between high and low DNA density regions. Different ATMp RIFs located at these interfaces are shown by color arrows in the different panels (note: an arrow of the same color represents the same focus). Panel C and D overlay the identified locations of ATMp and 53BP1 RIFs (green disk and red circles respectively) with the DAPI intensity and gradient images respectively. *Rdna* and *Rgrad* values are given for each panel with a colored text corresponding to the protein. One can see in panel D that the green RIFs shown by arrows are along high gradient contours, which are reflected by a high *Rgrad* value. In contrast, the red RIF seem to locate themselves fairly randomly over the full nucleus, as reflected with *Rdna* and *Rgrad* values closed to 1.

**Figure 9 Increased co-localization of DNA damage markers rapidly after exposure to radiation.**

Panel A is an analysis summary of γH2AX and ATMp co-localization with 53BP1 done in three-dimensions. Two RIFs are considered co-localized if the distance between their centers is less or equal to 0.48 μm. As described in the method, RIF centers are determined as the brightest pixel within each spot. The γH2AX co-localization is illustrated in panel B with representative images of different time points and different type of radiations. γH2AX and 53BP1 foci locations are shown as green disks and red circles, respectively. Co-localized centers are circled by a yellow contour on the image and the amount of γH2AX co-localization is reported for each image. Both exposure to gamma-rays (Cs) and 1 GeV/amu Fe are illustrated for the two different time periods considered after exposure to radiation (1-4 min and 5-10 min). Averages for Cs are based on 2 independent experiments whereas averages for Fe are based on 4 independent experiments. A T- test was performed and a P-value of 0.01 was computed between the firsț and second time period considered for γH2AX (statistical significance noted on the graph as *)

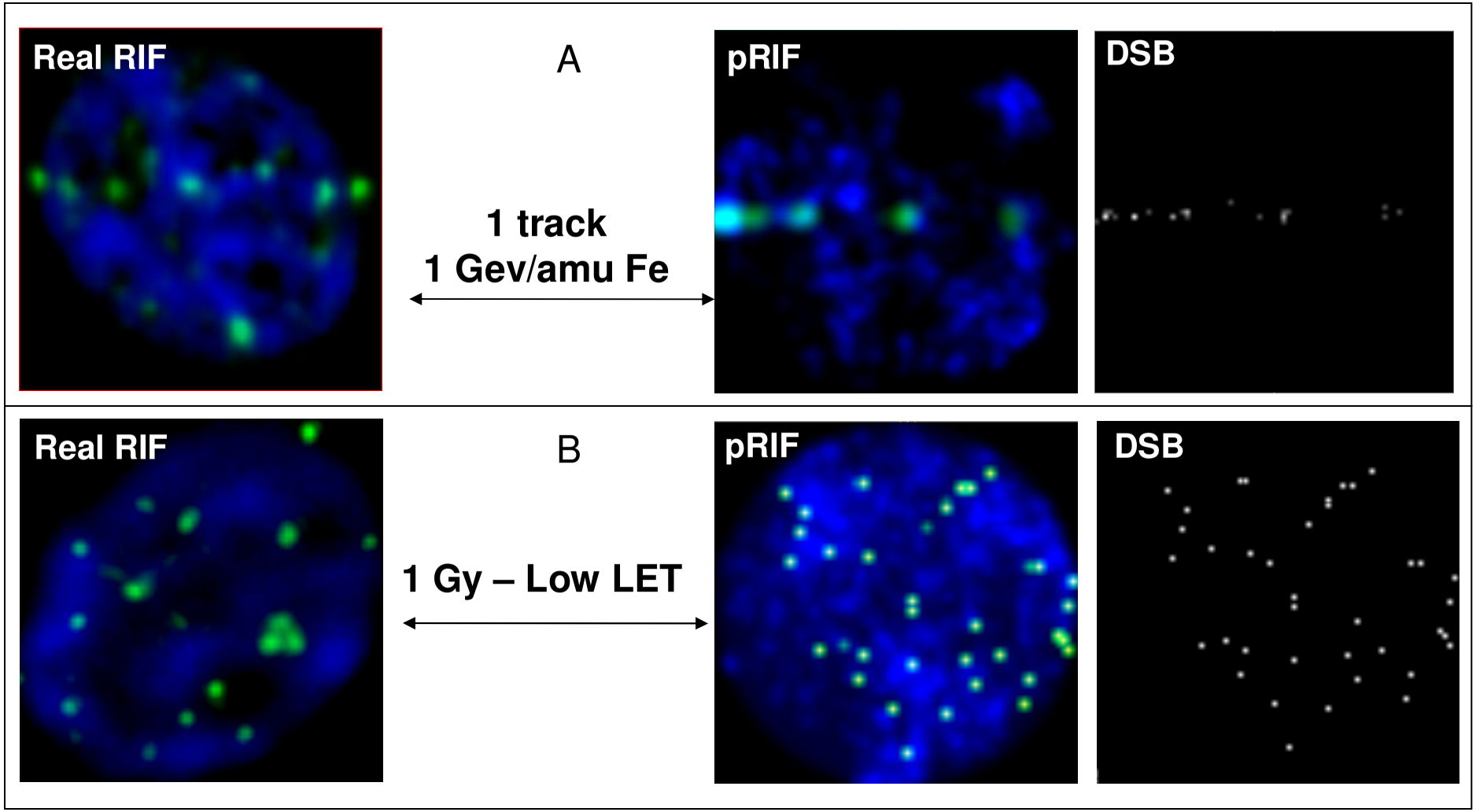
Real RIF
A
pRIF
DSB
1 track
1 Gev/amu Fe
Real RIF
B
pRIF
DSB
1 Gy – Low LET

**Figure 1**

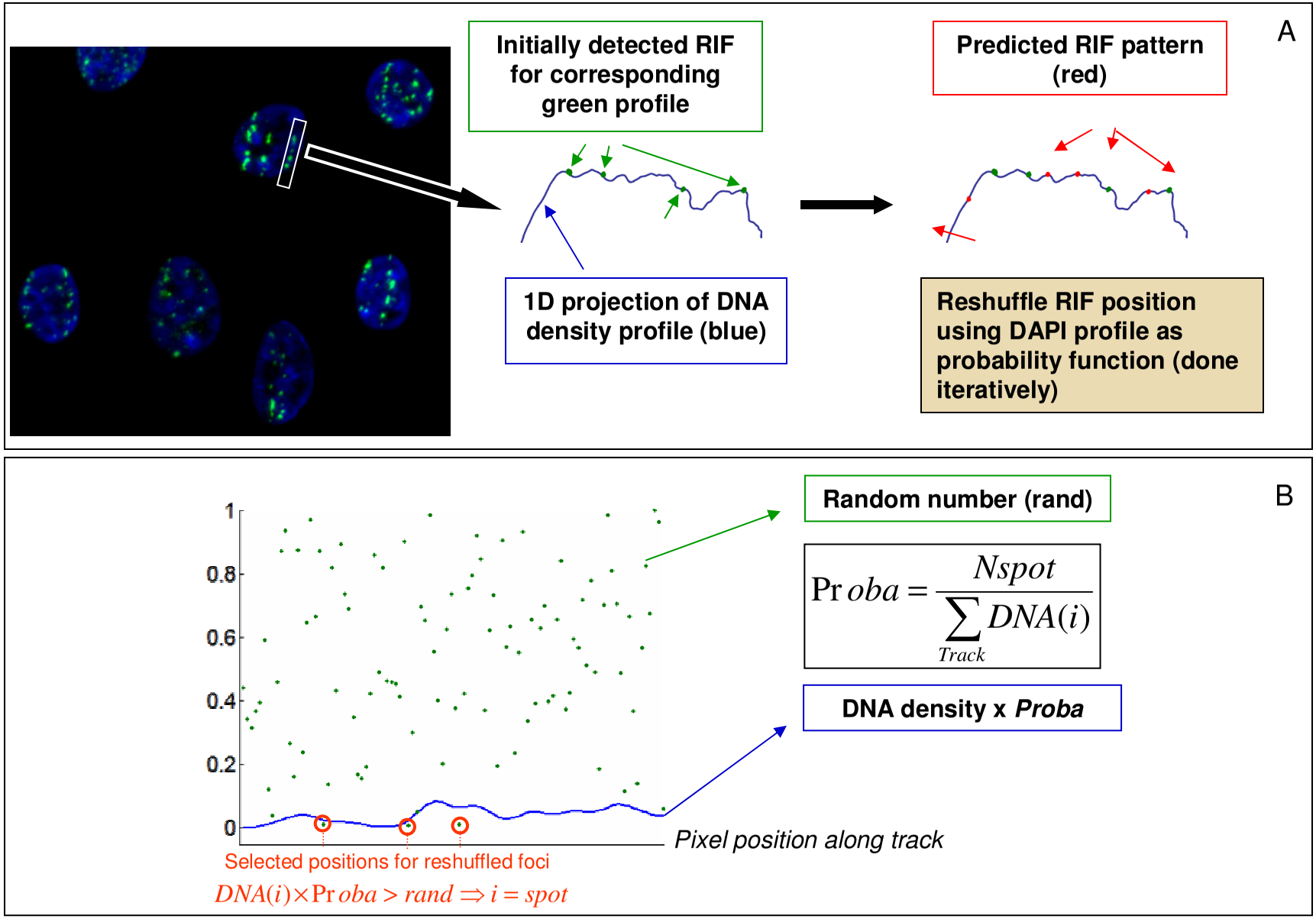
A
Initially detected RIF for corresponding green profile
Predicted RIF pattern (red)
1D projection of DNA density profile (blue)
Reshuffle RIF position using DAPI profile as probability function (done iteratively)
B
Random number (rand)
$\Pr oba = \frac{Nspot}{\sum_{Track} DNA(i)}$
DNA density x *Proba*
1
0.8
0.6
0.4
0.2
0
Pixel position along track
Selected positions for reshuffled foci
$DNA(i) \times \Pr oba > rand \Rightarrow i = spot$

**Figure 2**

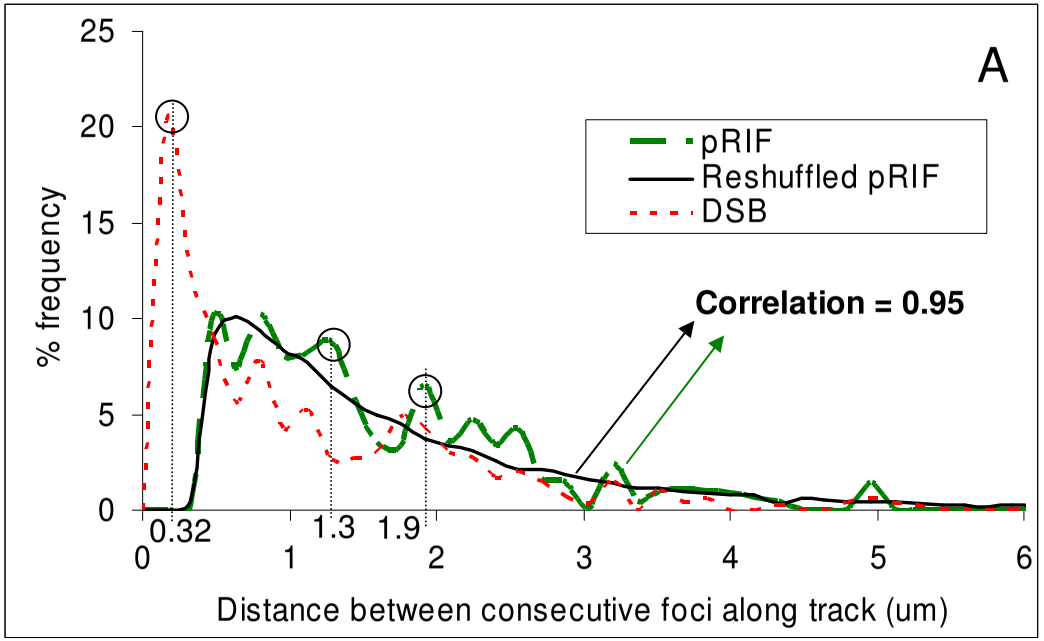


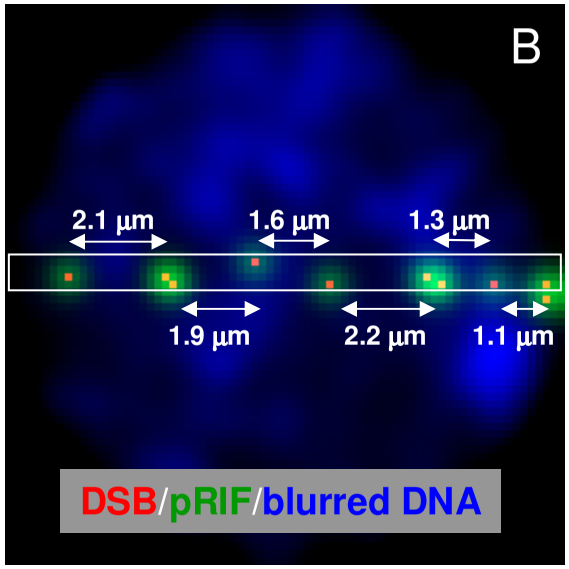


**Maximum Intensity Profile along white box**

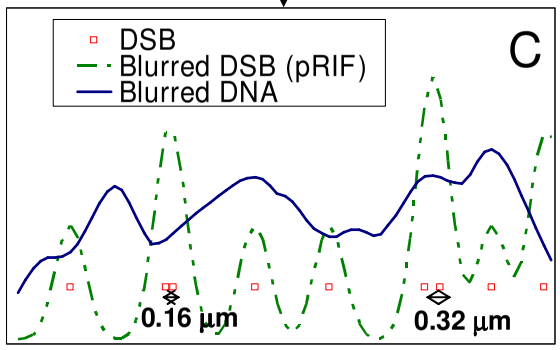


**Figure 3**

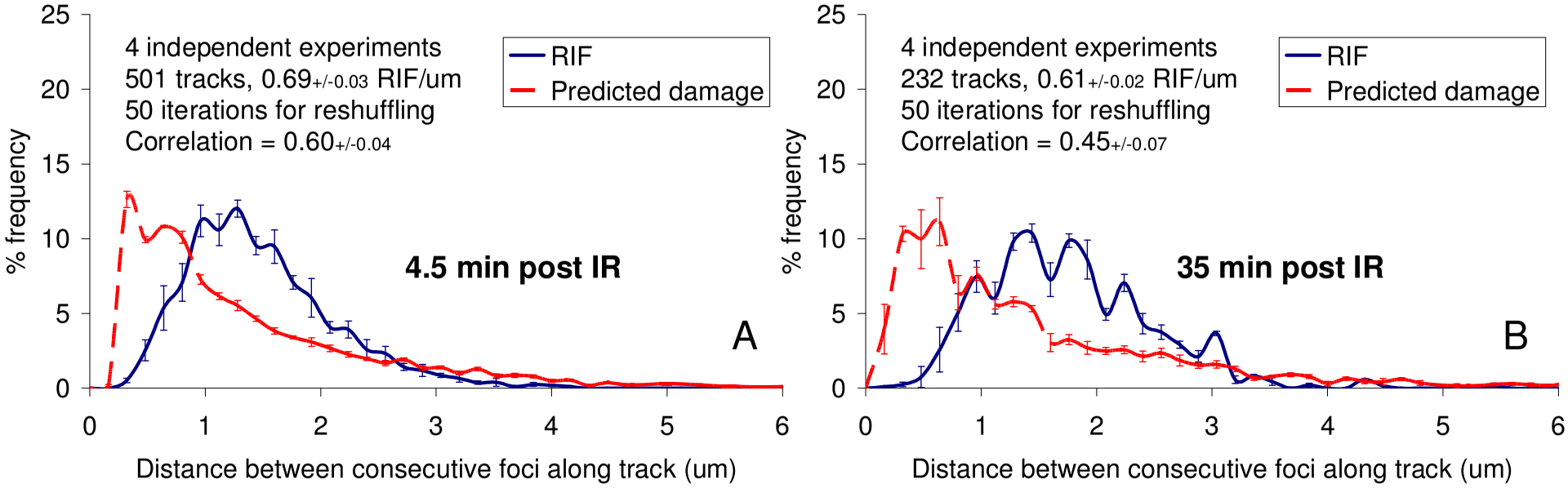
4 independent experiments
501 tracks, 0.69+/-0.03 RIF/um
50 iterations for reshuffling
Correlation = 0.60+/-0.04
RIF
Predicted damage
4.5 min post IR
A
% frequency
Distance between consecutive foci along track (um)
4 independent experiments
232 tracks, 0.61+/-0.02 RIF/um
50 iterations for reshuffling
Correlation = 0.45+/-0.07
RIF
Predicted damage
35 min post IR
B
% frequency
Distance between consecutive foci along track (um)

**Figure 4**

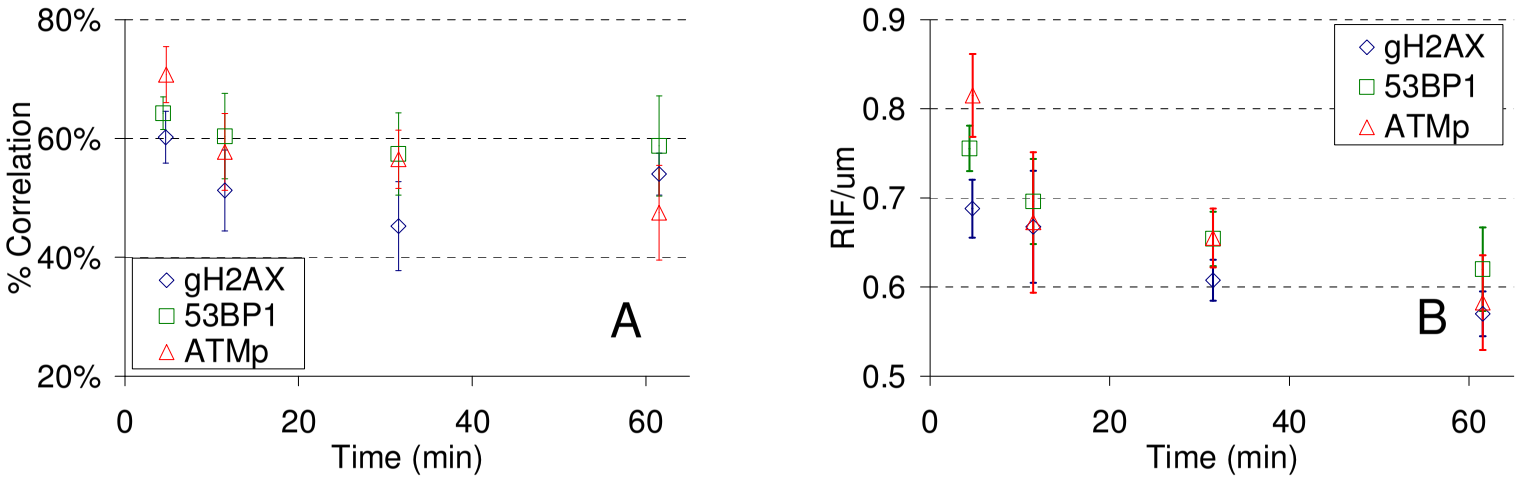
80%
60%
40%
20%
% Correlation
gH2AX
53BP1
ATMp
A
0
20
40
60
Time (min)
0.9
0.8
0.7
0.6
0.5
RIF/um
gH2AX
53BP1
ATMp
B
0
20
40
60
Time (min)

**Figure 5**

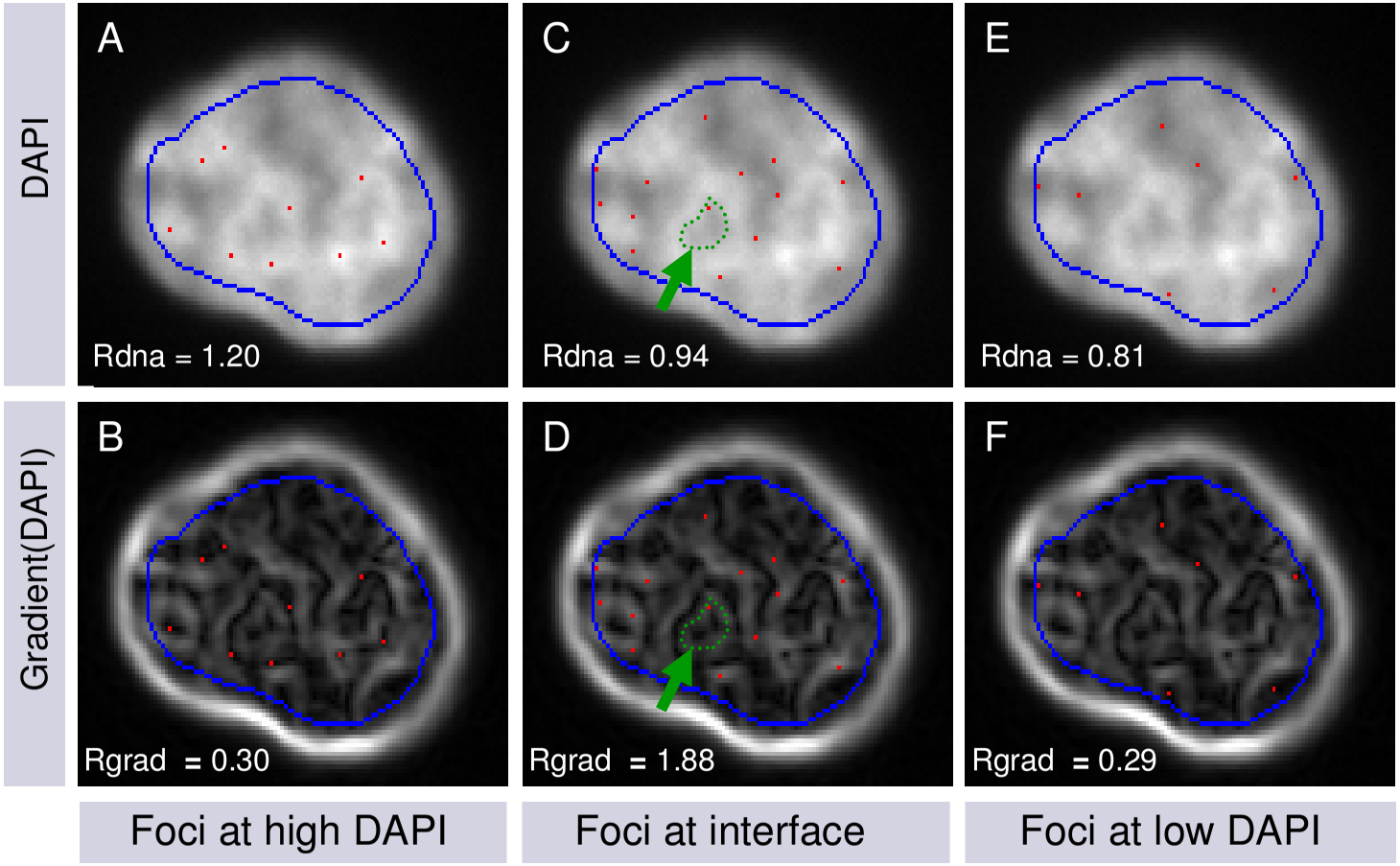
DAPI
Gradient(DAPI)
A
C
E
B
D
F
Rdna = 1.20
Rdna = 0.94
Rdna = 0.81
Rgrad = 0.30
Rgrad = 1.88
Rgrad = 0.29
Foci at high DAPI
Foci at interface
Foci at low DAPI

**Figure 6**

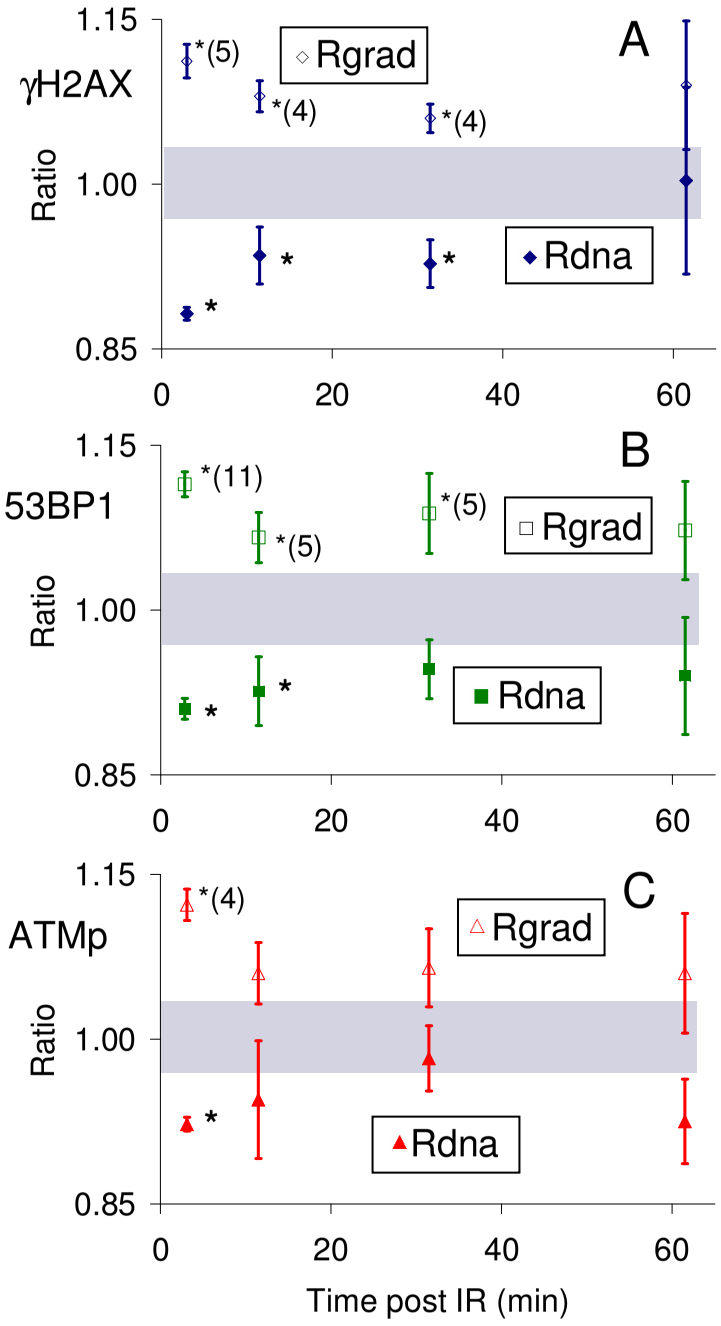
A
γH2AX
Ratio
1.15
1.00
0.85
*(5)
*(4)
*(4)
Rgrad
Rdna
0
20
40
60
B
53BP1
*(11)
*(5)
*(5)
C
ATMp
*(4)
Time post IR (min)

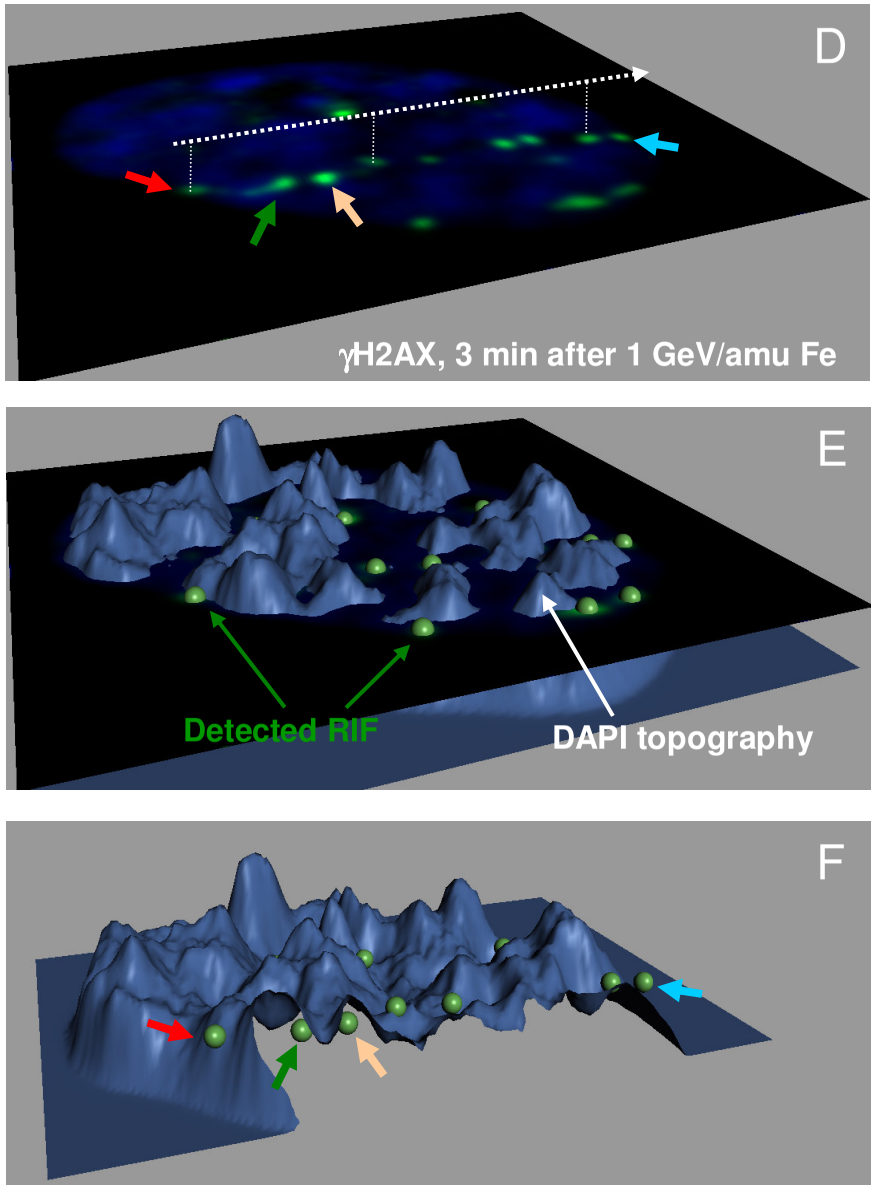
D
γH2AX, 3 min after 1 GeV/amu Fe
E
Detected RIF
DAPI topography
F

**Figure 7**

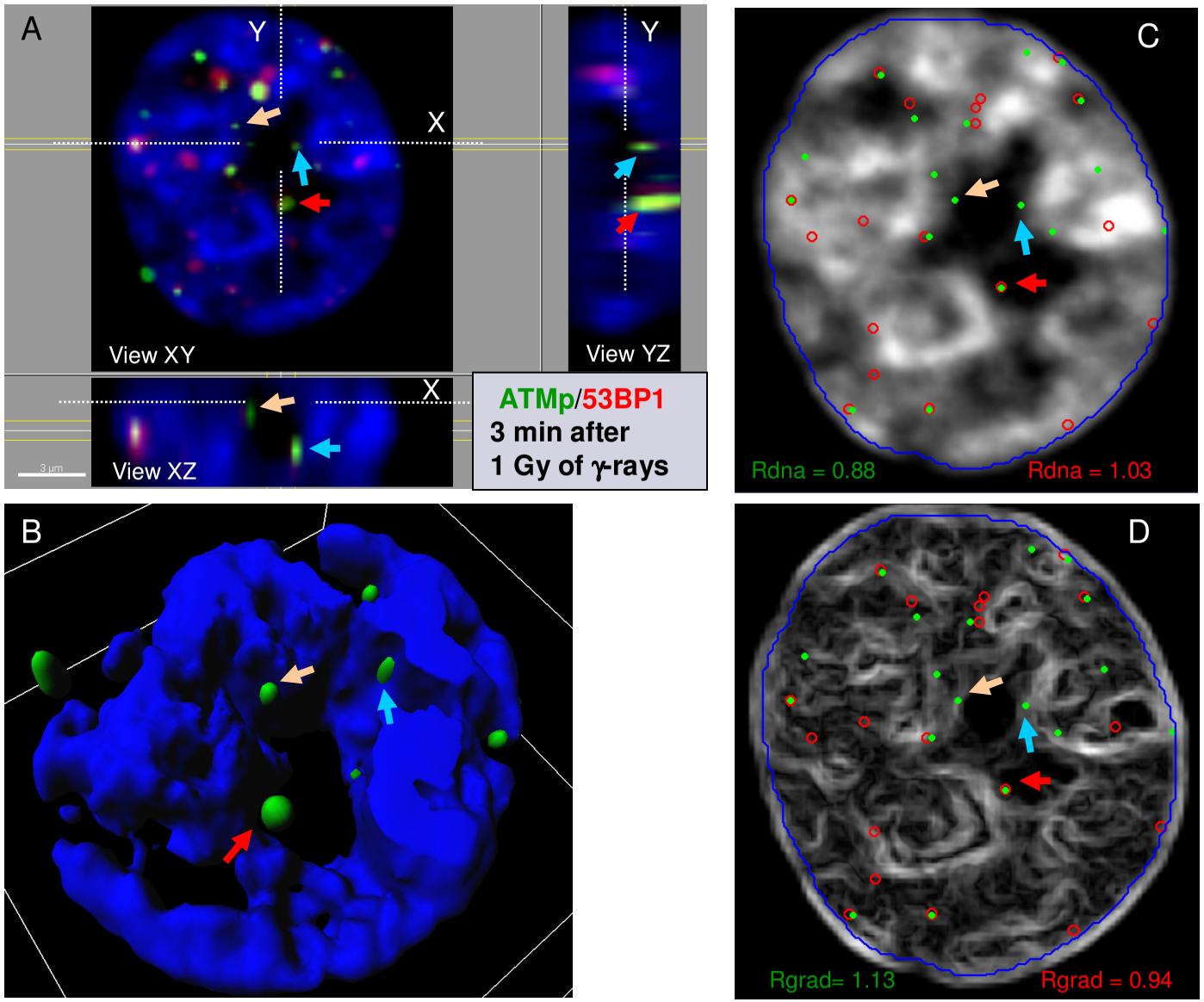
A
Y
X
View XY
Y
View YZ
X
View XZ
3 µm
ATMp/53BP1
3 min after
1 Gy of γ-rays
B
C
Rdna = 0.88
Rdna = 1.03
D
Rgrad= 1.13
Rgrad = 0.94

**Figure 8**

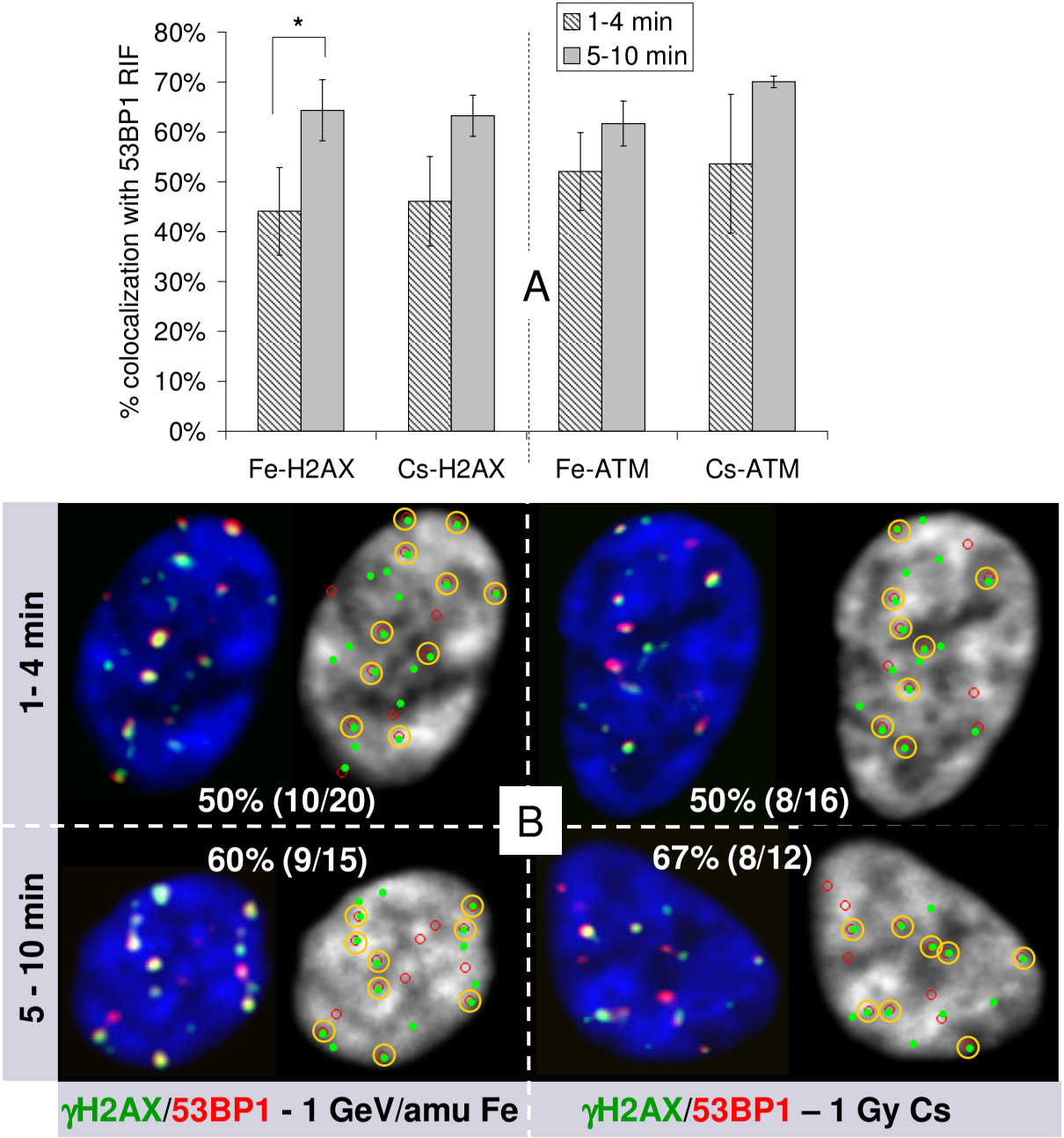
% colocalization with 53BP1 RIF
80%
70%
60%
50%
40%
30%
20%
10%
0%
*
1-4 min
5-10 min
A
Fe-H2AX
Cs-H2AX
Fe-ATM
Cs-ATM
1- 4 min
5 - 10 min
50% (10/20)
50% (8/16)
B
60% (9/15)
67% (8/12)
γH2AX/53BP1 - 1 GeV/amu Fe
γH2AX/53BP1 – 1 Gy Cs

**Figure 9**